J Sci Comput (2015) 64:837–857
DOI 10.1007/s10915-014-9950-x

A Fast Explicit Operator Splitting Method for Modified Buckley–Leverett Equations

Chiu-Yen Kao · Alexander Kurganov · Zhuolin Qu · Ying Wang

Received: 28 April 2014 / Revised: 18 October 2014 / Accepted: 5 November 2014 /
Published online: 22 November 2014

Abstract In this paper, we propose a fast explicit operator splitting method to solve the modified Buckley–Leverett equations which include a third-order mixed derivatives term resulting from the dynamic effects in the pressure difference between the two phases. The method splits the original equation into two equations, one with a nonlinear convective term and the other one with high-order linear terms so that appropriate numerical methods can be applied to each of the split equations: the high-order linear equation is numerically solved using a pseudo-spectral method, while the nonlinear convective equation is integrated using the Godunov-type central-upwind scheme. The spatial order of the central-upwind scheme depends on the order of the piecewise polynomial reconstruction: we test both the second-order minmod-based reconstruction and fifth-order WENO5 one to demonstrate that using higher-order spatial reconstruction leads to more accurate approximation of solutions. A variety of numerical examples in both one and two space dimensions show that the solutions may have many different saturation profiles depending on the initial conditions, diffusion parameter, and the third-order mixed derivatives parameter. The results are consistent with the study of traveling wave solutions and their bifurcation diagrams.

Keywords Buckley–Leverett equations · Modified Buckley–Leverett equations · Fast explicit operator splitting method · Central-upwind schemes · Pseudo-spectral methods · Minmod-based reconstruction · WENO5 reconstruction

C.-Y. Kao
Department of Mathematical Sciences, Claremont McKenna College, Claremont, CA 91711, USA
e-mail: Chiu-Yen.Kao@claremontmckenna.edu

A. Kurganov (✉) · Z. Qu
Mathematics Department, Tulane University, New Orleans, LA 70118, USA
e-mail: kurganov@math.tulane.edu

Z. Qu
e-mail: zqu1@tulane.edu

Y. Wang
Department of Mathematics, University of Oklahoma, Norman, OK 73019, USA
e-mail: wang@ou.edu

Mathematics Subject Classification 76M12 · 65M08 · 65M70 · 35L67 · 35L65

1 Introduction

The Buckley–Leverett (BL) equation was proposed in [2] to describe two-phase fluid flow in porous media. In particular, the BL equation is used to model the secondary oil recovery by water injection in oil reservoir. In the one-dimensional (1-D) case, the classical BL equation is a scalar conversation law:

$$u_t + F(u)_x = 0, \tag{1.1}$$

with the flux function $F(u) = f(u)$ defined as

$$f(u) = \begin{cases} 0, & u < 0, \\ \frac{u^2}{u^2 + M(1-u)^2}, & 0 \le u \le 1, \\ 1, & u > 1. \end{cases} \tag{1.2}$$

In this model, u denotes the water saturation, f is water fractional flow rate function and M is the viscosity ratio between water and oil. When a gravitational effect is taken into account, then a modified flux $F(u) = g(u)$, where

$$g(u) = f(u)(1 - C(1-u)^2), \tag{1.3}$$

and C is a positive constant, should be used.

Practically relevant initial data for the BL equation (1.1) are Riemann data:

$$u(x, 0) = \begin{cases} u_B, & x \le 0, \\ 0, & x > 0, \end{cases} \tag{1.4}$$

where u_B is a positive constant representing an initial water saturation in the fluid injected into the oil reservoir. It is well-known that the entropy solution of the initial value problem (IVP) (1.1)–(1.4) preserves the monotonicity of the initial data. However, the experiments [8, Figure 5] of two-phase flow in porous medium reveal complex infiltration profiles, which may involve an overshoot, that is, the water saturation may develop nonmonotone profiles even with the initial data being monotone. This suggests that the classical BL equation (1.1) needs to be modified.

In [1,11,12], the dynamic capillary pressure is introduced to derive the modified Buckley–Leverett (MBL) equation which includes a third-order mixed derivatives term (see Sect. 2). In the 1-D case, the MBL equation reads:

$$u_t + F(u)_x = \varepsilon u_{xx} + \varepsilon^2 \tau u_{xxt}, \qquad \varepsilon > 0, \quad \tau > 0, \tag{1.5}$$

where F is given by either (1.2) or (1.3). This equation is of pseudo-parabolic type. The existence condition for traveling wave solutions which violate the Oleinik entropy condition, that is, the so-called nonclassical solutions of (1.5) is discussed in [25]. The phase plane analysis is performed in [21] to study the properties of the traveling waves corresponding to undercompressive shocks. In [27], the finite domain and half-line problem are compared: The solution of the finite domain $[0, L]$ problem converges to that of the half-line $[0, \infty)$ problem exponentially fast as $L \to \infty$ in the sense of a weighted H^1-norm. Therefore, it provides justification to use the numerical solution on the finite domain to approximate the solution of the half-line problem.

When capturing solutions of both the classical BL and MBL equations numerically, one has to deal with the difficulties related to the fact that the fluxes (1.2) and (1.3) are nonconvex. As

it was demonstrated in [16], solutions of nonconvex (systems of) conservation laws computed by high-order methods may fail to resolve composite waves and thus may fail to converge to the entropy solution. To overcome this difficulty, a simple adaptive strategy was proposed in [16]: A more diffusive version of the scheme has to be applied near the flux inflection points (this is achieved by using a more diffusive nonlinear limiter there). When the MBL equation is integrated numerically, an additional difficulty is related to the presence of high-order terms on the right-hand side (RHS) of (1.5): It is well-known that in this case, explicit methods may be inefficient especially when a fine mesh is used to accurately capture small scale details of the solution.

Several numerical methods for the MBL equation have been proposed. In [25], a first order finite difference scheme was presented. A more accurate approach has been advocated in [27,28], where second- and third-order Godunov-type staggered central schemes were developed to capture the nonclassical solutions of the 1-D MBL equation (1.5).

The main goal of this paper is to develop a highly accurate and efficient method for (1.5) and then to extend it to a more numerically demanding 2-D case. Our approach is based on the fast explicit operator splitting method proposed in [4–6] to efficiently solve (systems of) convection-diffusion equations and incompressible Navier-Stokes equations.

The main idea of our method is to split the MBL equation (1.5) into two simpler equations: the nonlinear equation

$$(u - \varepsilon^2 \tau u_{xx})_t + F(u)_x = 0 \tag{1.6}$$

and the linear one:

$$u_t = \varepsilon u_{xx} + \varepsilon^2 \tau u_{xxt}. \tag{1.7}$$

We then solve the convection-type equation (1.6) using the Godunov-type central-upwind scheme [14,15], while the high-order linear equation (1.7) is integrated exactly using a pseudo-spectral framework as it was done in [4, Section 4]. The order of the central-upwind schemes is determined by the order of the piecewise polynomial reconstruction (see, e.g., [14,15]). We use both the second-order minmod-based piecewise linear and the fifth-order WENO5 reconstructions and demonstrate that the use of the higher-order spatial reconstruction leads to substantially higher resolution of nonclassical solutions. While the results obtained using the minmod-based piecewise linear reconstruction are comparable to those reported in [27,28], the proposed method combined with the fifth-order WENO5 reconstruction outperforms its counterparts as it is clearly demonstrated in our 1-D numerical experiments.

The organization of this paper is as follows. In Sect. 2, we revisit the 1-D MBL equation and derive the 2-D MBL equation. In Sect. 3, a fast explicit operator splitting method for both 1-D and 2-D MBL equations is introduced. Numerical accuracy verification of the proposed method is provided Sect. 4, where the performance of the fast explicit operator splitting method is tested on a number of 1-D and 2-D numerical examples.

2 Backgrounds

In this section, we re-derive the 1-D MBL equation (the Hassanizadeh-Gray model) and extend it to the 2-D case. We also discuss a classification of different types of solutions of the Riemann problem (1.5), (1.4).

2.1 One-Dimensional MBL Equation

Consider the two-phase water-oil flow in an isotropic and homogeneous porous medium. Let S_i $(i = \mathrm{o}, \mathrm{w})$ be the saturations of the oil and water phases, respectively. Then the conservation of mass yields

$$\phi \frac{\partial S_i}{\partial t} + \frac{\partial q_i}{\partial x} = 0, \qquad i = \mathrm{o}, \mathrm{w}, \tag{2.1}$$

where q_i denotes the specific discharge of oil/water and ϕ denotes the porosity of the medium. By Darcy's law [24], q_i is proportional to the gradient of the phase pressure P_i:

$$q_i = -k \frac{k_{ri}(S_i)}{\mu_i} \frac{\partial P_i}{\partial x}, \qquad i = \mathrm{o}, \mathrm{w}, \tag{2.2}$$

where k denotes the absolute permeability, $k_{r\mathrm{o}}$ and $k_{r\mathrm{w}}$ stand for the relative permeabilities of oil and water, respectively, and μ_o and μ_w denote their viscosities. The capillary pressure P_c defines the difference in the pressures of the two phases:

$$P_c = P_\mathrm{o} - P_\mathrm{w}.$$

In [1,11,12], the dynamic capillary pressure was defined as

$$P_c = p_c(S_\mathrm{w}) - \phi\tau \frac{\partial S_\mathrm{w}}{\partial t}, \tag{2.3}$$

where $p_c(S_\mathrm{w})$ is the *static* capillary pressure, τ is a positive constant and $\frac{\partial S_\mathrm{w}}{\partial t}$ is the dynamic effects. Assume that the medium is completely saturated, that is,

$$S_\mathrm{o} + S_\mathrm{w} = 1. \tag{2.4}$$

Combining (2.1)–(2.4), a general form of the MBL equation is (see [23,25,27] for details)

$$\frac{\partial u}{\partial t} + \frac{\partial F(u)}{\partial x} = -\frac{\partial}{\partial x}\left\{ H(u) \frac{\partial}{\partial x}\left(J(u) - \tau \frac{\partial u}{\partial t} \right) \right\}, \tag{2.5}$$

where $u = S_\mathrm{w}$ is the saturation of water, and F, H, J are functions of u; the flux function F is equal to either f given by (1.2) or g given by (1.3).

In this paper, we consider the MBL equation (1.5), which is a version of (2.5) with the linearized RHS, obtained by taking

$$H(u) = \varepsilon^2 \quad \text{and} \quad J(u) = -\frac{u}{\varepsilon},$$

see [23,25,27].

2.2 Two-Dimensional MBL Equation

In this section, we introduce a new 2-D MBL equation (the 2-D BL equation was derived in [29], also see [13]).

If we consider the flow where imbibition takes places under influence of gravity [7], then the mass balance gives

$$\phi \frac{\partial(\rho_i S_i)}{\partial t} + \nabla \cdot (\rho_i \boldsymbol{q}_i) = 0, \qquad i = \mathrm{o}, \mathrm{w},$$

where ρ_o and ρ_w denote the density of oil and water phases, both of which are considered to be incompressible, so

$$\phi \frac{\partial S_i}{\partial t} + \nabla \cdot (\boldsymbol{q}_i) = 0, \qquad i = o, w. \tag{2.6}$$

We again assume that the medium is completely saturated, that is, (2.4) is satisfied. This, in turn, gives

$$\nabla \cdot (\boldsymbol{q}_o + \boldsymbol{q}_w) = \nabla \cdot \boldsymbol{q} = 0. \tag{2.7}$$

Throughout this paper, we assume that $\boldsymbol{q} = \text{Const}$.

By Darcy's law, the momentum balance equation is

$$\boldsymbol{q}_i = \lambda_i (\nabla P_i + \rho_i \tilde{g} \boldsymbol{e}_z), \tag{2.8}$$

where

$$\lambda_i = -k \frac{k_{r_i}(S_i)}{\mu_i}, \tag{2.9}$$

$\tilde{g}$ is a gravitational constant and $\boldsymbol{e}_z$ is a unit vector in the z-direction.

Combining (2.6)–(2.8) with the same capillary pressure formulation (2.3), which was used in the 1-D case, the following model is obtained:

$$u_t + \nabla \cdot \left[f(u) \frac{\boldsymbol{q}}{\phi} - f(u)(1-u)^2 \frac{k(\rho_w - \rho_o)\tilde{g}}{\mu_o \phi} \boldsymbol{e}_z \right] = -\nabla \cdot \big[H(u) \nabla (J(u) - \tau u_t) \big], \tag{2.10}$$

where f is given by (1.2) with $M = \mu_w/\mu_o$,

$$H(u) = \frac{k}{\mu_o} f(u)(1-u)^2 \quad \text{and} \quad J(u) = \frac{p_c(u)}{\phi}.$$

This is a general form of the 2-D MBL equation, which can be rewritten as follows. We use $\boldsymbol{q} = (q_1, q_2)^T$ to rescale the space variables,

$$x \frac{\phi}{q_1} \to x, \quad z \frac{\phi}{q_2} \to z,$$

take $\phi = \mathcal{O}(\varepsilon)$, and denote

$$M := \frac{\mu_w}{\mu_o}, \quad C := \frac{k(\rho_w - \rho_o)\tilde{g}}{\mu_o q_2}.$$

Then, Eq. (2.10) reduces to

$$u_t + \nabla \cdot [f(u)(1,1)^T - C f(u)(1-u)^2 \boldsymbol{e}_z] = \varepsilon \Delta u + \varepsilon^2 \tau \Delta u_t,$$

which can be rewritten as

$$u_t + F(u)_x + G(u)_z = \varepsilon \Delta u + \varepsilon^2 \tau \Delta u_t \tag{2.11}$$

where $F(u) = f(u)$ and $G(u) = g(u)$ are given by (1.2) and (1.3), respectively. This equation is a modification of the classical 2-D BL equation

$$u_t + F(u)_x + G(u)_z = 0, \tag{2.12}$$

when the capillary pressure in (2.3) is taken to be constant.

2.3 Bifurcation Diagram

Our goal is to understand the nature of solutions of the Riemann problem (1.5), (1.4) for different values of the initial parameter u_B. To this end, we follow [25] and study the traveling wave solutions of (1.5).

For $\tau > 0$, we look for a traveling wave solution $u(\eta)$, where $\eta = (x - st)/\varepsilon$. Substituting $u(\eta)$ into (1.5) results in the following ODE:

$$-su' + (F(u))' = u'' - s\tau u'''. \tag{2.13}$$

This equation is to be solved subject to the boundary conditions at infinities,

$$u(-\infty) = u_B, \quad u(\infty) = 0, \tag{2.14}$$

which together with the Rankine–Hugoniot condition determine the traveling wave speed:

$$s = \frac{F(u_B) - F(0)}{u_B - 0} = \frac{F(u_B)}{u_B}.$$

We then integrate equation (2.13) over (η, ∞) and reduce the order by one:

$$-su + F(u) = u' - s\tau u''. \tag{2.15}$$

It was proved in [25] that existence of the traveling wave solution satisfying (2.15), (2.14) depends on the parameter τ in the following manner. There exists a critical value τ_F^* such that for all $\tau \in [0, \tau_F^*]$, there exists a solution of (2.15), (2.14) with $u_B = \alpha_F$, where α_F is the unique root of the equation

$$F'(u) = \frac{F(u)}{u}.$$

For $\tau > \tau_F^*$, there exists a unique value of $\widetilde{u} > \alpha_F$ such that the solution of the boundary value problem (BVP) (2.15), (2.14) with $u_B = \widetilde{u}$ exists. For $u_B < \widetilde{u}$, the solution of (2.15), (2.14) will exist only if $u_B < \underline{u}$, where $\underline{u}$ is the unique root of the following equation:

$$F(r) - \frac{F(\widetilde{u})}{\widetilde{u}}\, r = 0, \quad 0 < r < \widetilde{u}. \tag{2.16}$$

For a given τ, the values of $\widetilde{u}$ and $\underline{u}$ can be found as follows. Since the traveling wave (when exists) is a decreasing function of η, we perform the following change of variables: $z(u) = -u'(\eta(u))$, which transforms equation (2.15) into

$$s\tau z z' + z = su - F(u), \quad u \in (0, u_B). \tag{2.17}$$

Since we have assumed that $u(\eta)$ is decreasing, $z(u) > 0$ for all $u \in (0, u_B)$. Moreover,

$$z(0) = z(u_B) = 0. \tag{2.18}$$

We therefore need to find $u_B > \alpha_F$ satisfying the above conditions. This can be done by applying a shooting method to the BVP (2.17), (2.18), and the obtained u_B is the desired value of $\widetilde{u}$. After this, we can find the corresponding value of $\underline{u}$ by (numerically) solving equation (2.16).

We now take particular examples of $F = f$ given by (1.2) and $F = g$ given by (1.3) with $M = 1/2$ and $C = 2$ and numerically compute α_f, α_g, τ_f^*, τ_g^*, and the values of $\widetilde{u}$ and $\underline{u}$ for τ uniformly distributed in the interval $[0, 5]$. The obtained results are summarized in the bifurcation diagram shown in Fig. 1. Notice that when $\tau \le \tau^*$, both $\widetilde{u}$ and $\underline{u}$ are equal to α.

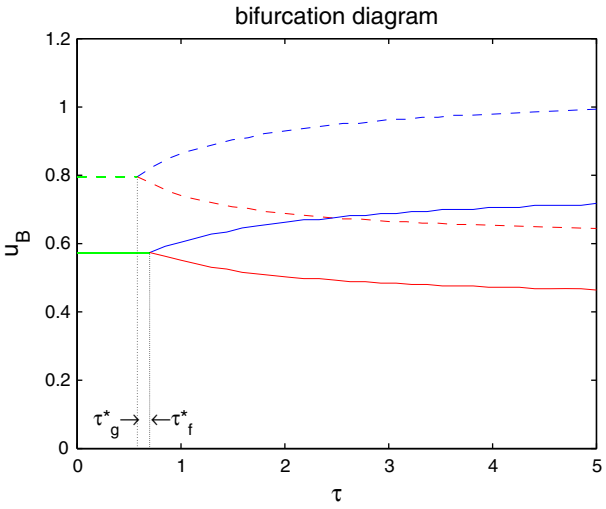

Fig. 1 Bifurcation diagram in the (τ, u_B)-space for the flux functions f (*solid lines*) and g (*dashed lines*). For both f and g, the *upper curves* represent $\widetilde{u}$ and the *lower curves* represent $\underline{u}$

Based on the bifurcation diagram in Fig. 1, three qualitatively different types of solution profiles of the Riemann problem (1.5), (1.4) are possible (all of them are illustrated in the numerical examples presented in Sect. 4):

(i) If $u_B > \widetilde{u}$, then the left state u_B is connected to $\widetilde{u}$ through a rarefaction wave, followed by a shock that jumps from $\widetilde{u}$ down to 0;
(ii) If $\underline{u} < u_B < \widetilde{u}$, then the solution jumps up from u_B to $\widetilde{u}$ through a shock, and then jumps down from $\widetilde{u}$ to 0 through another shock;
(iii) If $u_B < \underline{u}$, then the solution consists of a single shock that connects u_B with 0.

Remark 2.1 Notice that nonclassical solutions of the Riemann problem (1.5), (1.4) will correspond to nonmonotone solutions of the BVP (2.15), (2.14), obtained in Case (ii) above.

3 Fast Explicit Operator Splitting Method

There are many numerical methods for convection-diffusion equations, which arise in a wide variety of applications. However, in the convection dominated case, many schemes either have extensive numerical viscosity, which makes the solution under-resolved, or introduce spurious oscillations near sharp shock profiles. An attempt to preserve a delicate balance between the convection and diffusion terms was made in [3–6], where a fast explicit operator splitting method was proposed. In this section, we will use the same splitting idea to design new numerical schemes for the MBL equations. For the sake of brevity, we will only present the 1-D method (its extension to the 2-D case is rather straightforward).

3.1 Splitting Strategy

To apply splitting methods, we first combine the time derivative terms, that is, we rewrite the MBL equation (1.5) as

$$(u - \varepsilon^2 \tau u_{xx})_t + F(u)_x = \varepsilon u_{xx}. \tag{3.1}$$

We then split equation (3.1) into two simpler equations: the nonlinear convection-type equation

$$(u - \varepsilon^2 \tau u_{xx})_t + F(u)_x = 0 \tag{3.2}$$

and the linear diffusion-type equation

$$(u - \epsilon^2 \tau u_{xx})_t = \varepsilon u_{xx}, \tag{3.3}$$

and denote the exact solution operators associated with Eqs. (3.2) and (3.3) by $S_{\mathcal{N}}$ and $S_{\mathcal{L}}$, respectively.

Let us assume that at time t, the solution of the original MBL equation (3.1) is available. We then introduce a time step Δt and evolve the solution from t to $t + \Delta t$ using the second-order Strang splitting method:

$$u(x, t + \Delta t) = S_{\mathcal{N}}\left(\frac{\Delta t}{2}\right) S_{\mathcal{L}}\left(\Delta t\right) S_{\mathcal{N}}\left(\frac{\Delta t}{2}\right) u(x, t) + \mathcal{O}((\Delta t)^3).$$

To implement the splitting method in practice, the exact solution operators $S_{\mathcal{N}}$ and $S_{\mathcal{L}}$ are to be replaced by their numerical approximations. Our particular choice of the required nonlinear and linear solvers are described in Sects. 3.2 and 3.3, respectively.

3.2 Central-Upwind Schemes for Equation (3.2)

In order to develop a numerical method for the nonlinear convection-type equation (3.2), we first introduce an intermediate variable v and rewrite equation (3.2) as a system of two equations:

$$v_t + F(u)_x = 0, \tag{3.4}$$

$$u - \varepsilon^2 \tau u_{xx} = v. \tag{3.5}$$

We then solve Eq. (3.4) using a semi-discrete finite-volume method. To this end, we introduce a uniform spatial grid $x_\alpha := \alpha \Delta x$, the finite volume cells $I_j := [x_{j-\frac{1}{2}}, x_{j+\frac{1}{2}}]$, and the cell averages

$$\bar{v}_j(t) := \frac{1}{\Delta x} \int\limits_{I_j} v(x, t) dx,$$

which are evolved in time by solving the following systems of ODEs:

$$\frac{d}{dt} \bar{v}_j(t) = -\frac{H_{j+\frac{1}{2}}(t) - H_{j-\frac{1}{2}}(t)}{\Delta x}, \tag{3.6}$$

where $H_{j+\frac{1}{2}}$ are numerical fluxes. We use the central-upwind fluxes proposed in [15]:

$$H_{j+\frac{1}{2}}(t) := \frac{a^+_{j+\frac{1}{2}} F\left(u^-_{j+\frac{1}{2}}\right) - a^-_{j+\frac{1}{2}} F\left(u^+_{j+\frac{1}{2}}\right)}{a^+_{j+\frac{1}{2}} - a^-_{j+\frac{1}{2}}} + \frac{a^+_{j+\frac{1}{2}} a^-_{j+\frac{1}{2}}}{a^+_{j+\frac{1}{2}} - a^-_{j+\frac{1}{2}}} \left[u^+_{j+\frac{1}{2}} - u^-_{j+\frac{1}{2}}\right], \tag{3.7}$$

where all of the quantities on the RHS depend on time, but from now on we omit this dependence for the sake of brevity.

In (3.7), $u^{\pm}_{j+\frac{1}{2}}$ are the right- left-sided point values of the piecewise polynomial reconstruction of u at $x = x_{j+\frac{1}{2}}$. This reconstruction is obtained from the cell averages $\bar{u}_j(t) := \frac{1}{\Delta x} \int_{I_j} u(x, t)\, dx$, which are assumed to be available at time t. A formal spatial

order of the semi-discrete scheme (3.6), (3.7) is determined by the formal order of the reconstruction. In this paper, we use either a second-order scheme obtained with the help of a generalized minmod-based reconstruction (see [17,18,22,26]) or a fifth-order scheme, for which the values of $u^{\pm}_{j+\frac{1}{2}}$ are computed using the WENO5 approach (see, e.g., [19,20]). The right- and left-sided local speeds of propagation, $a^{\pm}_{j+\frac{1}{2}}$, are determined using the following estimates (see [16]):

$$a^{+}_{j+\frac{1}{2}} = \max\left\{\max_{u\in\left[m_{j+\frac{1}{2}},M_{j+\frac{1}{2}}\right]}\{F'(u)\},0\right\},\quad a^{-}_{j+\frac{1}{2}} = \min\left\{\min_{u\in\left[m_{j+\frac{1}{2}},M_{j+\frac{1}{2}}\right]}\{F'(u)\},0\right\},$$

where $m_{j+\frac{1}{2}} := \min\{u^{-}_{j+\frac{1}{2}}, u^{+}_{j+\frac{1}{2}}\}$ and $M_{j+\frac{1}{2}} := \max\{u^{-}_{j+\frac{1}{2}}, u^{+}_{j+\frac{1}{2}}\}$.

Finally, a fully discrete scheme for (3.4) is obtained by applying an ODE solver to the ODE system (3.6). In our numerical experiments, we have used the third-order strong stability preserving Runge–Kutta (SSP-RK) method (see [9,10]).

At each stage of SSP-RK method, as long as the new values of v are obtained, the elliptic equation (3.5) is to be solved to update u. Since (3.5) is a linear equation with the periodic boundary conditions, it can be exponentially accurately and efficiently solved using the pseudo-spectral method. To do so, we first use the Fast Fourier Transform (FFT) algorithm to compute the discrete Fourier coefficients $\{\widehat{v}_m\}$ from the cell averages $\{\bar{v}_j\}$ and substitute the Fourier expansions

$$u(x) = \sum_m \widehat{u}_m e^{imx} \quad \text{and} \quad v(x) = \sum_m \widehat{v}_m e^{imx}$$

into (3.5). We then obtain a simple algebraic equation for the discrete Fourier coefficients $\widehat{u}_m$:

$$\widehat{u}_m - \varepsilon^2\tau(ik)^2\widehat{u}_m = \widehat{v}_m,$$

and thus,

$$\widehat{u}_m = \frac{\widehat{v}_m}{1+\varepsilon^2\tau k^2},$$

for all m. At the end, we recover the cell averages $\{\bar{u}_j\}$ from the Fourier coefficients $\{\widehat{u}_m\}$ using the inverse FFT algorithm.

Remark 3.1 As it has been mentioned in Sect. 1, the solution computed by a high-order central-upwind scheme may fail to resolve composite waves and thus may not converge to the entropy solution. This was discovered in [16], where a simple adaptive strategy was proposed to overcome this difficulty: A more diffusive nonlinear limiter (the most diffusive minmod limiter [17,18,22,26] with the parameter 1) has to be applied near the flux inflection points. We have implemented this adaptive strategy to compute the numerical solutions presented in Sect. 4, but in fact it was not necessary in any of the studied numerical examples. Therefore, in Sect. 4, we present the results obtained by the direct implementation of the central-upwind scheme described here.

3.3 Pseudo-Spectral Method for Equation (3.3)

Since Eq. (3.3) is linear, a pseudo-spectral method would lead to a highly accurate approximation of the solution operator $S_{\mathcal{L}}$. Similarly to the way Eq. (3.5) was solved in Sect. 3.2,

we first use the FFT algorithm to compute the discrete Fourier coefficients $\{\widehat{u}_m\}$ from the available cell averages $\{\bar{u}_j\}$ and approximate u at time t by its Fourier expansion:

$$u(x,t) \approx \sum_m \widehat{u}_m(t)\, e^{imx}.$$

Substituting this into (3.3) results in the following simple linear ODEs for the discrete Fourier coefficients:

$$\frac{d}{dt}\left[\widehat{u}_m(t) - \varepsilon^2\tau(ik)^2\widehat{u}_m\right] = \varepsilon(ik)^2\widehat{u}_m,$$

which can be solved exactly on the time interval $(t, t+\Delta t]$ for any Δt:

$$\widehat{u}_m(t+\Delta t) = \exp\left(\frac{-\varepsilon k^2\Delta t}{1+\varepsilon^2\tau k^2}\right)\widehat{u}_m(t).$$

Finally, we use the inverse FFT algorithm to obtain the cell averages of the solution at the new time level, $\{\bar{u}_j(t+\Delta t)\}$, out of the set of its discrete Fourier coefficients $\{\widehat{u}_m(t+\Delta t)\}$.

Remark 3.2 In this paper, we restrict our consideration to periodic boundary conditions only. If other boundary conditions are prescribed, the proposed method still applies with the only exception that the FFT and inverse FFT algorithms are to be replaced with the Fast Chebyshev Transform and inverse Fast Chebyshev Transform in the solutions of both Eqs. (3.5) and (3.3).

4 Numerical Results

In this section, we test the performance of the proposed fast explicit operator splitting method on several 1-D and 2-D examples. In the 1-D examples, we compare the results obtained by applying the second-order minmod-based reconstruction and the fifth-order WENO5 approach on several different grids to demonstrate that higher-order spatial reconstruction leads to much higher resolution of computed solutions. We also compare the behavior of solutions of Eq. (1.5) with different nonlinear fluxes (1.2) and (1.3). The obtained results are consistent with the traveling wave results presented in the bifurcation diagrams in Fig. 1. In the 2-D examples, we only use a more computationally efficient and accurate WENO5 reconstruction.

In all of the examples below, the periodic boundary conditions are imposed, the diffusion coefficient is $\varepsilon = 10^{-3}$, and the minmod parameter $\theta = 1.3$ is chosen. More precisely, the minmod derivative of a grid function $\{\psi_j\}$ is

$$(\psi_x)_j = \text{minmod}\left(\theta\,\frac{\psi_{j+1}-\psi_j}{\Delta x},\ \frac{\psi_{j+1}-\psi_{j-1}}{2\Delta x},\ \theta\,\frac{\psi_j-\psi_{j-1}}{\Delta x}\right),$$

where the minmod function is defined by

$$\text{minmod}(z_1, z_2, \ldots) := \begin{cases} \min(z_1, z_2, \ldots), & \text{if } \ z_i > 0 \ \ \forall i, \\ \max(z_1, z_2, \ldots), & \text{if } \ z_i < 0 \ \ \forall i, \\ 0, & \text{otherwise.} \end{cases}$$

4.1 Linear Accuracy Tests

In this section, we test the accuracy and convergence of the proposed 1-D and 2-D methods by solving the MBL equations (1.5) and (2.11) with the linear fluxes, for which the exact

Table 1 The 1-D linear accuracy test using the minmod-based reconstruction

N	L^1-error	Rate	L^2-error	Rate	L^∞-error	Rate
64	1.4755E−02	–	1.3400E−02	–	2.4467E−02	–
128	2.6529E−03	2.4755	2.4454E−03	2.4541	5.9092E−03	2.0498
256	4.5606E−04	2.5403	3.7676E−04	2.6983	9.7694E−04	2.5966
512	1.0240E−04	2.1551	8.0050E−05	2.2347	1.1068E−04	3.1418
1,024	2.5122E−05	2.0272	1.9691E−05	2.0233	1.9653E−05	2.4936
2,048	6.2732E−06	2.0017	4.9248E−06	1.9994	4.9236E−06	1.9969

Table 2 The 1-D linear accuracy test using the WENO5 reconstruction

N	L^1-error	Rate	L^2-error	Rate	L^∞-error	Rate
64	1.3145E−05	–	1.0293E−05	–	1.0782E−05	–
128	8.6308E−07	3.9289	6.7674E−07	3.9269	6.7037E−07	4.0076
256	8.3592E−08	3.3681	6.5634E−08	3.3661	6.4986E−08	3.3667
512	9.6942E−09	3.1082	7.6128E−09	3.1079	7.5732E−09	3.1012
1,024	1.1924E−09	3.0233	9.3638E−10	3.0233	9.3454E−10	3.0186
2,048	1.5306E−10	2.9617	1.2021E−10	2.9616	1.2057E−10	2.9544

solutions can be easily obtained using the spectral method (to compute the errors reported in Tables 1, 2 and 3 below we used the truncated spectral solutions with the number of modes equal to the number of grid cells used to generate the corresponding numerical solutions).

We begin with the 1-D case and consider the following IVP:

$$\begin{cases} u_t + u_x = \varepsilon u_{xx} + 5\varepsilon^2 u_{xxt}, & (x,t) \in (0,2) \times (0,2], \\ u(x,0) = \sin(\pi x), & x \in [0,2]. \end{cases}$$

In Tables 1 and 2, we show the errors and experimental convergence rates achieved with the second-order minmod-based and fifth-order WENO5 reconstructions, respectively. The errors, measured in both the L^1-, L^2- and L^∞-norms, confirm the expected convergence rates. The second-order minmod-based reconstruction leads to the second-order experimental convergence, while the fifth-order WENO5 reconstruction increase the convergence rate to the third one. We would also like to point out that the absolute size of the obtained WENO5 errors is about 3–4 orders of magnitude smaller than the minmod ones.

We note that in the WENO5 case, the convergence rates are limited by the accuracy of the third-order SSP-RK solver and the second-order Strang splitting algorithm. The latter, however, does not affect the obtained rates even for large number of grid cells (N) since the splitting errors are very small thanks to the smallness of the diffusion coefficient ε (according to the error estimates obtained in [4–6], the splitting error is expected to be proportional to $\varepsilon^3(\Delta t)^2$).

In the 2-D accuracy test, we consider the 2-D IVP,

$$\begin{cases} u_t + u_x + u_y = \varepsilon \Delta u + 5\varepsilon^2 (\Delta u)_t, & (x,y) \in (0,2) \times (0,2), \quad t \in (0,2], \\ u(x,y,0) = \sin(\pi x) + \sin(\pi y), & (x,y) \in (0,2) \times (0,2), \end{cases}$$

which is numerically solved using the fast explicit operator splitting method utilizing the WENO5 reconstruction. As in the 1-D case, the expected experimental third-order convergence rate is achieved, as one can see in Table 3.

Table 3 The 2-D linear accuracy test using the WENO5 reconstruction

N	L^1-error	Rate	L^2-error	Rate	L^∞-error	Rate
64×64	3.3396E−05	–	2.0586E−05	–	2.1565E−05	–
128×128	2.1915E−06	3.9297	1.3535E−06	3.9269	1.3407E−06	4.0076
256×256	2.1273E−07	3.3648	1.3127E−07	3.3661	1.2997E−07	3.3667
512×512	2.4679E−08	3.1077	1.5226E−08	3.1079	1.5146E−08	3.1012
$1{,}024 \times 1{,}024$	3.0370E−09	3.0226	1.8736E−09	3.0226	1.8690E−09	3.0185

Table 4 The nonlinear accuracy test using the minmod-based reconstruction

N	L^1-error	Rate	L^2-error	Rate	L^∞-error	Rate
64	5.1709E−03	–	1.1041E−02	–	4.9341E−02	–
128	1.7538E−03	1.5600	5.1379E−03	1.1036	3.5078E−02	0.4922
256	5.3929E−04	1.7013	1.9756E−03	1.3789	1.8171E−02	0.9490
512	1.4631E−04	1.8821	6.1700E−04	1.6790	6.7943E−03	1.4192
1,024	3.6482E−05	2.0038	1.6260E−04	1.9239	2.0300E−03	1.7429
2,048	8.8589E−06	2.0420	3.9584E−05	2.0383	5.0771E−04	1.9994

4.2 Nonlinear Accuracy Test

In this section, we test the accuracy and convergence of the proposed 1-D methods by solving the MBL equation (1.5) with the nonlinear flux.

Consider the following IVP:

$$\begin{cases} u_t + f(u)_x = \varepsilon u_{xx} + 0.2\varepsilon^2 u_{xxt}, & (x,t) \in (0,2) \times (0, 0.125], \\ u(x,0) = 0.45(\sin(\pi x) + 1), & x \in [0,2]. \end{cases}$$

where f is given by (1.2) with $M = 2$. In Tables 4 and 5, we show the errors and experimental convergence rates achieved with the second-order minmod-based and fifth-order WENO5 reconstructions, respectively. The corresponding reference solutions are obtained by computing the numerical solutions on a very fine grid with $N = 16384$, and the errors are measured in both the L^1-, L^2- and L^∞-norms. Compared with the results obtained with linear flux in Sect. 4.1, the convergence rates here are lower due to the nonlinearity in the flux f and presence of sharp gradient areas in the solution, see Fig. 2. However, the fifth-order WENO5 reconstruction still leads to slightly higher experimental convergence rates and smaller errors than the second-order minmod-based reconstruction does.

4.3 High-Resolution Via the WENO5 Reconstruction

In this section, we show that the use of the fifth-order WENO5 reconstruction leads to much more accurate and efficient method compared with the one that utilizes the second-order minmod-based reconstruction.

We consider the 1-D MBL equation (1.5), (1.2) with the initial condition

$$u(x,0) = \begin{cases} u_B, \text{ if } & x \in (0.75, 2.25), \\ 0, & \text{otherwise} \end{cases} \qquad x \in [0,3].$$

Table 5 The nonlinear accuracy test using the WENO5 reconstruction

N	L^1-error	Rate	L^2-error	Rate	L^∞-error	Rate
64	2.8837E−03	–	7.5782E−03	–	4.0485E−02	–
128	8.6877E−04	1.7309	3.1722E−03	1.2564	2.2508E−02	0.8469
256	2.0925E−04	2.0538	9.6753E−04	1.7131	8.8667E−03	1.3440
512	3.9587E−05	2.4021	1.9185E−04	2.3344	2.0925E−03	2.0832
1,024	7.7174E−06	2.3588	3.1650E−05	2.5997	3.5922E−04	2.5422
2,048	1.7354E−06	2.1529	6.5627E−06	2.2698	6.8772E−05	2.3850

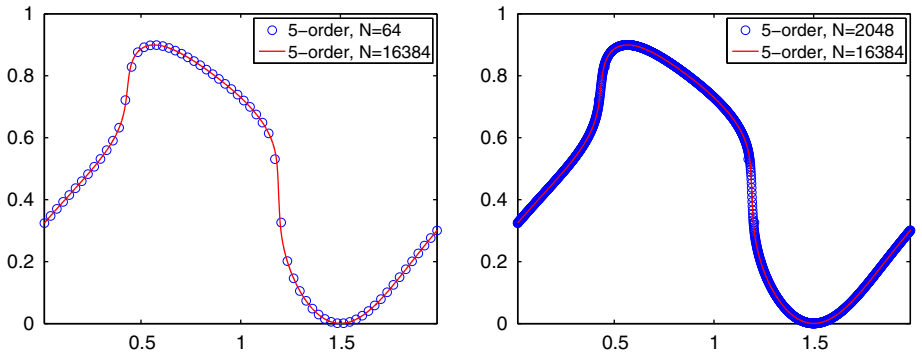

Fig. 2 Nonlinear accuracy test: solutions computed using the fifth-order WENO5 reconstructions on three different grids at the final time $T = 0.125$

We set the parameter M in flux (1.2) to be $M = 1/2$ and compute the solution at the final time $T = 0.5$ for three different sets of values of τ and u_B that correspond to three qualitatively different solutions.

Example 1 $\tau = 3.5, u_B = 0.85 > \widetilde{u}$

The first pair (τ, u_B) corresponds to Case (i) according to the bifurcation diagram in Fig. 1, see Sect. 2.3. One can prove that the right part of the exact solution consists of a rarefaction wave for $x \in [2.315, 2.711]$, which is connected to a plateau of height $\widetilde{u} \approx 0.698$, which is then followed by a shock at $x \approx 2.893$.

The solutions computed using both the second- and fifth-order reconstructions are shown in Fig. 3 (left). To check the accuracy of the obtained solutions, we need to verify how accurate the predicted plateau height is. We therefore zoom in at the plateau area and show the details of the computed solutions in Fig. 3 (right). As one can see, the plateau height, computed using the WENO5 reconstruction is more accurate even than the plateau height computed using the minmod-based reconstruction on a much finer grid.

Example 2 $\tau = 5, \underline{u} < u_B = 0.66 < \widetilde{u}$

The second pair of (τ, u_B) corresponds to Case (ii) according to the bifurcation diagram in Fig. 1, see Sect. 2.3. The exact solution is now completely different from the one in Example 1: its right part consists of a jump up (located at $x \approx 2.597$) to a plateau of height $\widetilde{u} \approx 0.713$ and a jump down (located at $x \approx 2.881$) to 0. This is a nonclassical (nonmonotone) solution, which is hard to capture since numerical diffusion would typically reduce the height of the

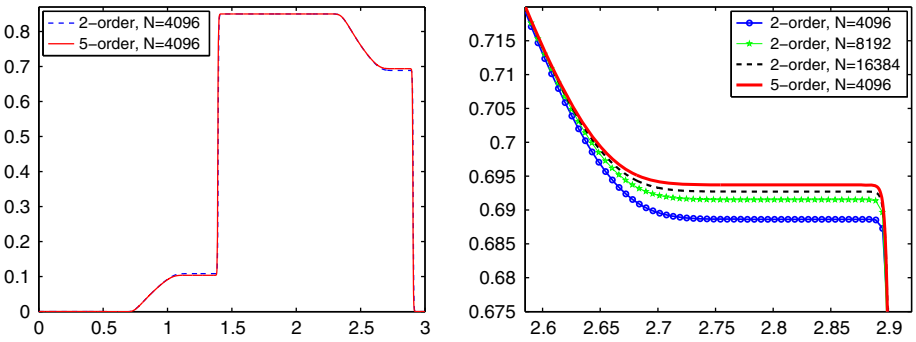

Fig. 3 Example 1: solutions computed using the second-order minmod-based and fifth-order WENO5 reconstructions (*left*); zoom in at the plateau area (*right*)

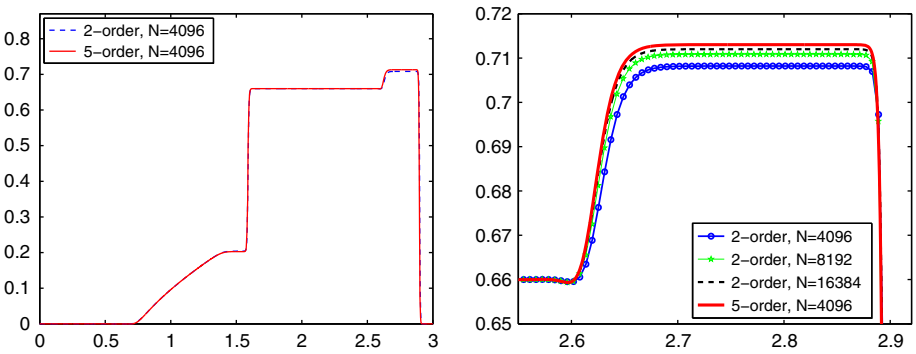

Fig. 4 Example 2: solutions computed using the second-order minmod-based and fifth-order WENO5 reconstructions (*left*); zoom in at the plateau area (*right*)

newly created plateau. Once again, the use of the WENO5 reconstruction leads to a much more accurate computed solution, see Fig. 4.

Example 3 $\tau = 5, \underline{u} < u_B = 0.52 < \widetilde{u}$

In the third example, we take another pair of (τ, u_B), which still corresponds to Case (ii) according to the bifurcation diagram in Fig. 1, but with a smaller value of u_B, which makes the solution nature to be slightly different. Namely, the connection between the u_B state and the plateau (which still has the same height as in Example 2) is nonmonotone since the exact solution now develops an oscillatory part around $x = 2.8$. As in Examples 1 and 2, one can see that the results obtained with the help of the WENO5 reconstruction are more accurate than the minmod results, see Fig. 5.

4.3.1 Computational Cost

To perform a fair comparison between the two versions of the proposed fast explicit operator splitting method, we compare their CPU times, which are recorded in Table 6. As one can see, for a fixed grid, the use of the WENO5 reconstruction increases the computational cost by about 35 %. However, it is clear that to achieve the same quality of resolution with the minmod-based reconstruction, one needs to use a substantially finer mesh, which makes the WENO5-based method to be not only more accurate, but also more efficient.

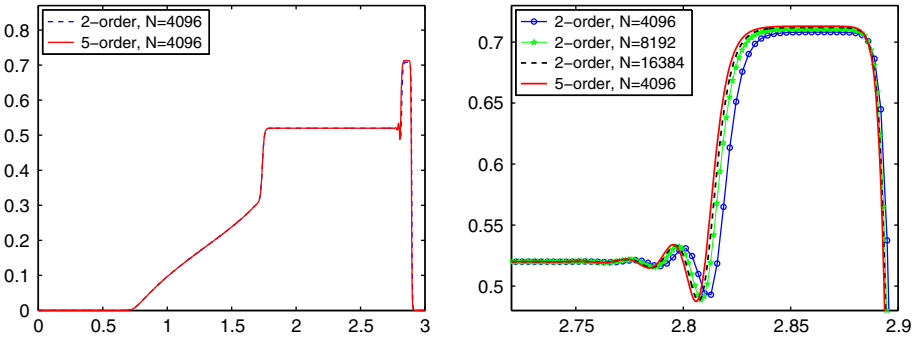

Fig. 5 Example 3: solutions computed using the second-order minmod-based and fifth-order WENO5 reconstructions (*left*); zoom in at the plateau area (*right*)

Table 6 Examples 1–3: comparison of the CPU times

N	Example 1		Example 2		Example 3	
	Minmod	WENO5	Minmod	WENO5	Minmod	WENO5
1,024	1.3572	1.9812	1.3884	2.0124	1.3728	2.0280
2,048	5.8656	8.4085	6.3492	8.2525	5.8500	8.4865
4,096	25.8494	36.2234	25.8962	35.7398	25.6778	36.0674
8,192	112.6483	151.3210	111.6499	151.2274	108.9511	151.9762
16,384	476.3802	617.8264	474.6018	630.4156	470.7018	627.5422

Table 7 The values of (τ, u_B) pairs used in the nine experiments reported in Fig. 7

(0.2, 0.85)	(0.65, 0.85)	(3.5, 0.85)
(0.2, 0.68)	(0.65, 0.68)	(3.5,0.68)
(0.2, 0.55)	(0.65, 0.55)	(3.5, 0.55)

4.4 Numerical Study of the Gravitational Effects

In this section, we study the gravitational effects by comparing the numerical solutions of the MBL equation (1.5) subject to the following initial data:

$$u(x,0) = \begin{cases} u_B, & \text{if } \ x \in (4,10), \\ 0, & \text{otherwise} \end{cases} \qquad x \in [0,13], \tag{4.1}$$

but with two different fluxes, $F = f$ and $F = g$, given by (1.2) and (1.3), respectively (recall that the g flux is obtained from the f flux when the gravity is taken into account). We take the flux parameters $M = 1/2$ and $C = 2$, and test the behavior of the solutions for nine representative pairs (τ, u_B) given in Table 7 and also marked by "$\times$" signs in Fig. 6. The solutions obtained by the fast explicit operator splitting method using the fifth-order WENO5 reconstruction are shown in Fig. 7. In all of the nine cases, the solutions behave exactly the way predicted by the bifurcation diagram and the computed plateau values are in good agreement with the analytical ones.

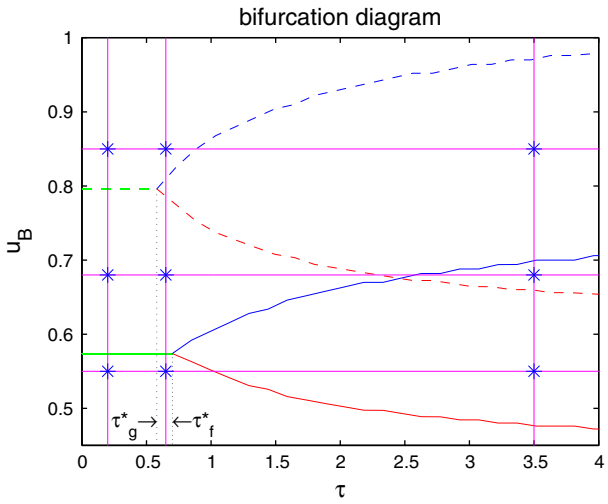

Fig. 6 The zoom-in view of the bifurcation diagram given in Fig. 1 along with the parameter values (marked by "×" signs) chosen in the nine experiments reported in Fig. 7

4.5 2-D Examples

In this section, we test the performance of the proposed fast explicit operator splitting method on two 2-D examples. Our goal is to clearly demonstrate the difference in the solutions of the BL and MBL equations. To achieve high resolution, we use the fifth-order WENO5 reconstruction.

Example 4 Rotational BL and MBL equations

We first consider the 2-D rotational BL,

$$u_t + \nabla \cdot (\boldsymbol{V} f(u)) = 0, \tag{4.2}$$

and MBL equations:

$$u_t + \nabla \cdot (\boldsymbol{V} f(u)) = \varepsilon \Delta u + \varepsilon^2 \tau \Delta u_t, \tag{4.3}$$

where f is given by (1.2), $M = 2$, $\tau = 5$ and $\boldsymbol{V}(x, z) = (z, -x)^T$. We select the computational domain to be $[-2, 2] \times [-2, 2]$ and prescribe the following initial condition:

$$u(x, z, 0) = \begin{cases} \sqrt{\dfrac{2}{3}}, & \text{if } \ x^2 + z^2 \le 1, \ x > 0, \ z > 0, \\ 0, & \text{otherwise.} \end{cases}$$

The solutions of the BL equation (4.2) and MBL equation (4.3) computed at time $T = 1.5$ using a uniform 512×512 grid are shown in Figs. 8 and 9, respectively. As one can see, the solution of the MBL equation develops a plateau at the rotational shock front, as one can expect based on the traveling wave analysis described in Sect. 2.3.

Example 5 Two-dimensional BL and MBL equations with gravitation

In the final example, we solve the following 2-D BL equation (2.12) and the MBL equation (2.11) with the fluxes $F(u) = f(u)$ and $G(u) = g(u)$ given by (1.2) and (1.3), respectively,

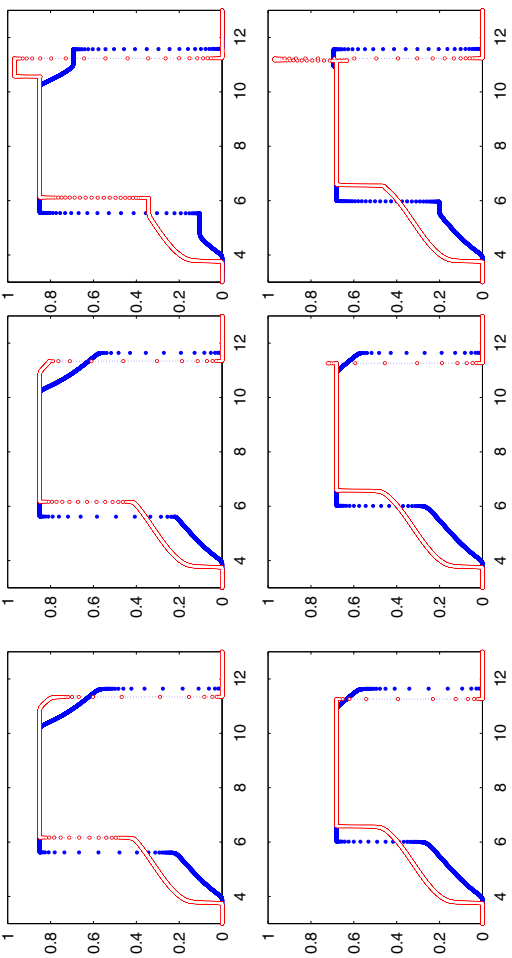

Fig. 7 Solutions of the MBL equation (1.5) with the f flux (1.2) (*filled circles*) and g flux (1.3) (*empty circles*) computed at time $T = 1.2$ using $N = 16{,}384$. For each of the *nine plots*, the initial data (4.1) corresponds to the nine (τ, u_B) pairs given in Table 7 and also marked in Fig. 6

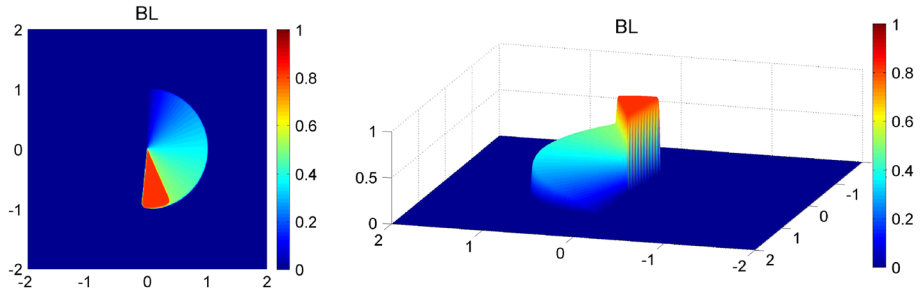

Fig. 8 Example 4: solution of the BL equation: *top* (*left*) and 3-D (*right*) views

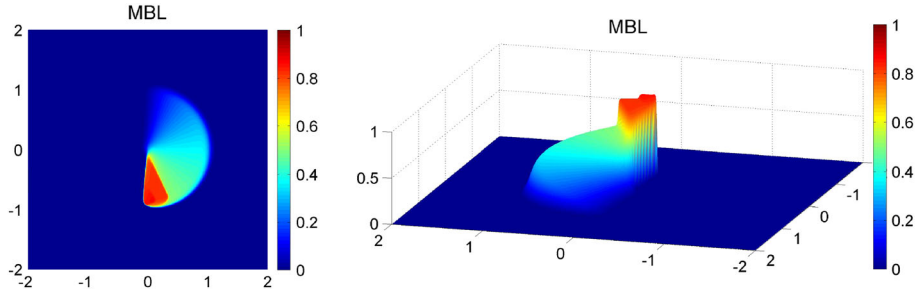

Fig. 9 Example 4: solution of the MBL equation: *top* (*left*) and 3-D (*right*) views

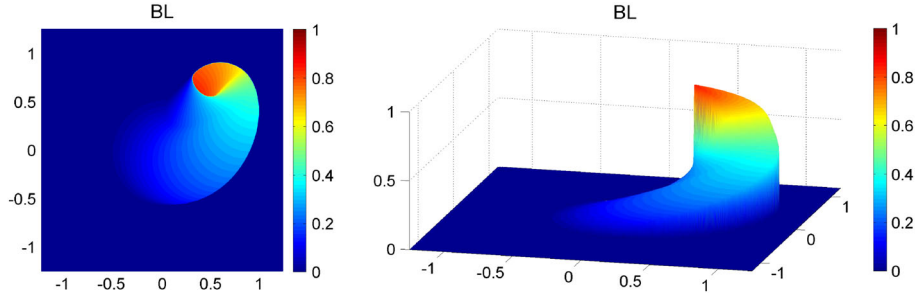

Fig. 10 Example 5, initial condition (4.4): Solution of the BL equation: *top* (*left*) and 3-D (*right*) views

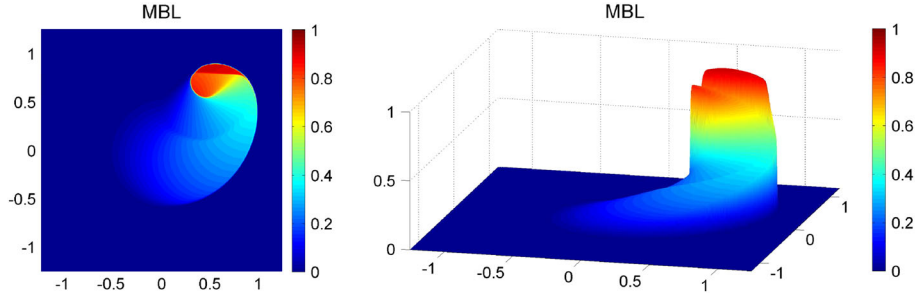

Fig. 11 Example 5, initial condition (4.4): solution of the MBL equation: *top* (*left*) and 3-D (*right*) views

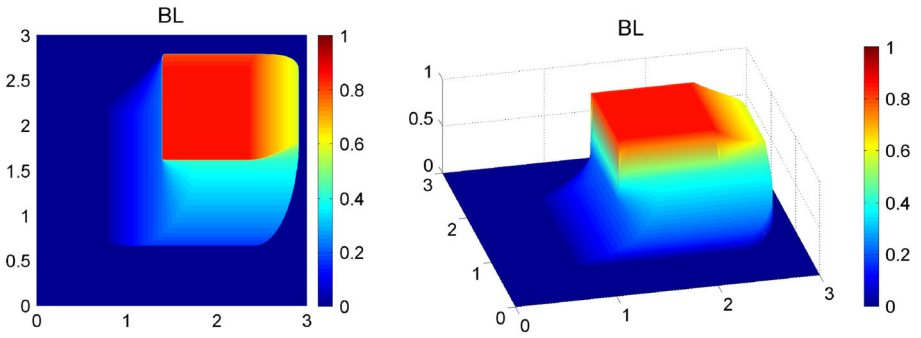

Fig. 12 Example 5, initial condition (4.5): Solution of the BL equation: top (*left*) and 3-D (*right*) views

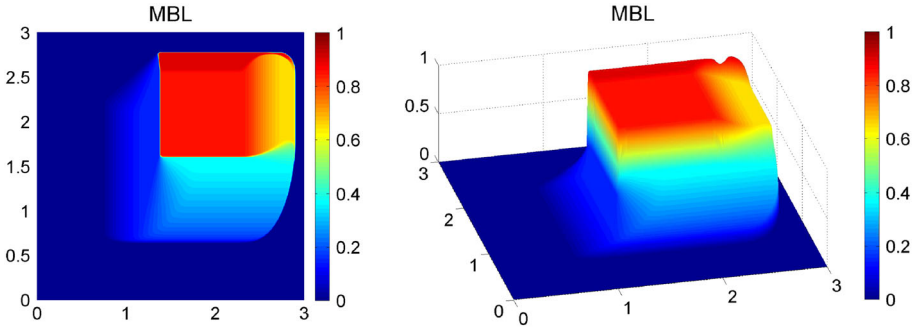

Fig. 13 Example 5, initial condition (4.5): Solution of the MBL equation: *top* (*left*) and 3-D (*right*) views

with $M = 1/2$, $C = 2$ and $\tau = 2.5$. We study two different initial conditions: a smooth 2-D Gaussian cut off by a plateau at the level $u = 0.85$,

$$u(x, z, 0) = 5e^{-20(x^2+z^2)}, \tag{4.4}$$

considered on the square computational domain $[-1.25, 1.25] \times [-1.25, 1.25]$, and a non-smooth

$$u(x, z, 0) = \begin{cases} 0.85, & \text{if} \quad 0.75 \le |x| \le 2.25, \quad 0.75 \le |z| \le 2.25, \\ 0, & \text{otherwise}, \end{cases} \tag{4.5}$$

considered on the square computational domain $[0, 3] \times [0, 3]$. Both solutions are computed on a uniform $1{,}024 \times 1{,}024$ grid at time $T = 0.48$.

Figures 10 and 11 show the results for the IVPs (2.12), (1.2), (1.3), (4.4) and (2.11), (1.2), (1.3), (4.4), respectively. Again, as one can expect, the solution of the MBL equation (2.11) generates a clear plateau across the shock front in the z-direction, which is consistent with the traveling wave study presented in Sect. 2.3, according to which the parameter pair $(\tau, u_B) = (2.5, 0.85)$ falls into Case (i) for the flux f and into Case (ii) for the flux g.

Finally, if we use the initial condition (4.5), the results obtained for the BL equation (2.12), (1.2), (1.3) and MBL equation (2.11), (1.2), (1.3) are shown in Figs. 12 and 13, respectively. Similarly to the previous case of the initial condition (4.4), the new plateau can be found near the shock front in the z-direction. However, because of the rarefaction wave created by the flux f in the x-direction, this plateau gets deformed at its upper-right corner.

Acknowledgments The work of C.-Y. Kao was supported in part by the NSF Grant DMS-1318364. The work of A. Kurganov and Z. Qu was supported in part by the NSF Grant DMS-1115718.

References

1. Barenblatt, G.I., Garcia-Azorero, J., De Pablo, A., Vazquez, J.L.: Mathematical model of the non-equilibrium water-oil displacement in porous strata. Appl. Anal. **65**, 19–45 (1997)
2. Buckley, S.E., Leverett, M.C.: Mechanism of fluid displacement in sands. Pet. Trans. AIME **146**, 107–116 (1942)
3. Chertock, A., Kashdan, E., Kurganov, A.: Propagation of Diffusing Pollutant by a Hybrid Eulerian–Lagrangian method, in Hyperbolic Problems: Theory, Numerics, Applications. Springer, Berlin (2008)
4. Chertock, A., Kurganov, A.: On splitting-based numerical methods for convection-diffusion equations. In: Numerical Methods for Balance Laws, vol. 24 of Quad. Mat., pp. 303–343. Department of Mathematics, Seconda University, Napoli, Caserta (2009)
5. Chertock, A., Kurganov, A., Petrova, G.: Fast explicit operator splitting method. Application to the polymer system. In: Finite Volumes for Complex Applications IV, pp. 63–72. ISTE, London (2005)
6. Chertock, A., Kurganov, A., Petrova, G.: Fast explicit operator splitting method for convection-diffusion equations. Int. J. Numer. Methods Fluids **59**, 309–332 (2009)
7. Cuesta, C., van Duijn, C.J., Hulshof, J.: Infiltration in porous media with dynamic capillary pressure: travelling waves. Eur. J. Appl. Math. **11**, 381–397 (2000)
8. DiCarlo, D.A.: Experimental measurements of saturation overshoot on infiltration. Water Resour. Res. **40**, W04215.1–W04215.9 (2004)
9. Gottlieb, S., Ketcheson, D., Shu, C.-W.: Strong Stability Preserving Runge–Kutta and Multistep Time Discretizations. World Scientific, Hackensack (2011)
10. Gottlieb, S., Shu, C.-W., Tadmor, E.: Strong stability-preserving high-order time discretization methods. SIAM Rev. **43**, 89–112 (2001)
11. Hassanizadeh, S., Gray, W.G.: Thermodynamic basis of capillary pressure in porous media. Water Resour. Res. **29**, 3389–3405 (1993)
12. Hassanizadeh, S.M., Gray, W.G.: Mechanics and thermodynamics of multiphase flow in porous media including interphase boundaries. Adv. Water Resour. **13**, 169–186 (1990)
13. Johnson, I.W., Wathen, A.J., Baines, M.J.: Moving finite element methods for evolutionary problems. II. Applications. J. Comput. Phys. **79**, 270–297 (1988)
14. Kurganov, A., Lin, C.-T.: On the reduction of numerical dissipation in central-upwind schemes. Commun. Comput. Phys. **2**, 141–163 (2007)
15. Kurganov, A., Noelle, S., Petrova, G.: Semidiscrete central-upwind schemes for hyperbolic conservation laws and Hamilton–Jacobi equations. SIAM J. Sci. Comput. **23**, 707–740 (2001). (electronic)
16. Kurganov, A., Petrova, G., Popov, B.: Adaptive semi-discrete central-upwind schemes for nonconvex hyperbolic conservation laws. SIAM J. Sci. Comput. **29**, 2381–2401 (2007)
17. Lie, K.-A., Noelle, S.: On the artificial compression method for second-order nonoscillatory central difference schemes for systems of conservation laws. SIAM J. Sci. Comput. **24**, 1157–1174 (2003)
18. Nessyahu, H., Tadmor, E.: Nonoscillatory central differencing for hyperbolic conservation laws. J. Comput. Phys. **87**, 408–463 (1990)
19. Shu, C.-W.: Essentially non-oscillatory and weighted essentially non-oscillatory schemes for hyperbolic conservation laws. In: Advanced Numerical Approximation of Nonlinear Hyperbolic Equations (Cetraro, 1997) vol. 1697 of Lecture Notes in Mathematics, pp. 325–432. Springer, Berlin (1998)
20. Shu, C.-W.: High order weighted essentially nonoscillatory schemes for convection dominated problems. SIAM Rev. **51**, 82–126 (2009)
21. Spayd, K., Shearer, M.: The Buckley-Leverett equation with dynamic capillary pressure. SIAM J. Appl. Math. **71**, 1088–1108 (2011)
22. Sweby, P.K.: High resolution schemes using flux limiters for hyperbolic conservation laws. SIAM J. Numer. Anal. **21**, 995–1011 (1984)
23. van Duijn, C.J., Mikelic, A., Pop, I.S.: Buckley-Leverett, Effective, equations by homogenization. In: Progress in Industrial Mathematics at ECMI 2000 (Palermo), vol. 1 of Math. Ind., pp. 2–51. Springer, Berlin (2002)
24. van Duijn, C.J., Mikelić, A., Pop, I.S.: Effective equations for two-phase flow with trapping on the micro scale. SIAM J. Appl. Math. **62**, 1531–1568 (2002). (electronic)
25. van Duijn, C.J., Peletier, L.A., Pop, I.S.: A new class of entropy solutions of the Buckley-Leverett equation. SIAM J. Math. Anal. **39**, 507–536 (2007). (electronic)

26. van Leer, B.: Towards the ultimate conservative difference scheme. V. A second-order sequel to Godunov's method. J. Comput. Phys. **32**, 101–136 (1979)
27. Wang, Y.: Central schemes for the modified Buckley-Leverett equation. PhD thesis, The Ohio State University (2010)
28. Wang, Y., Kao, C.-Y.: Central schemes for the modified Buckley-Leverett equation. J. Comput. Sci. **4**, 12–23 (2013)
29. Wathen, A.J.: Moving finite elements and oil reseruoir modelàng. PhD thesis, University of Reading, UK (1984)